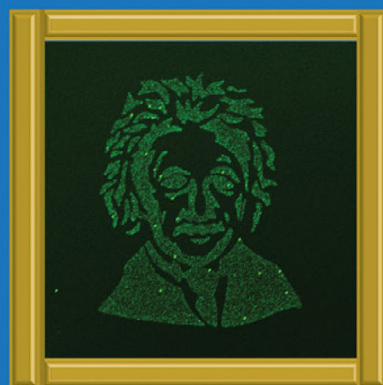
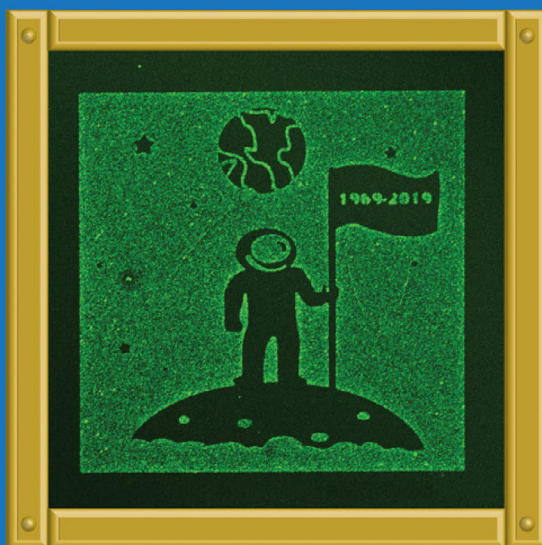
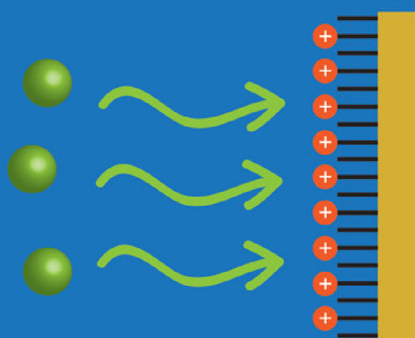
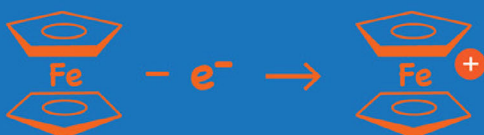
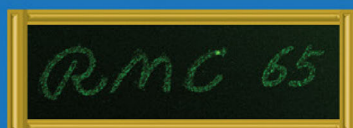


FUNDAMENTALS & APPLICATIONS

CHEMELECTROCHEM

ANALYSIS & CATALYSIS, BIO & NANO, ENERGY & MORE

100 μm



5/2020

Cover Feature:

M. S. Iqbal and W. Zhan

Electrochemically Triggered Interfacial Deposition/Assembly
of Aqueous-Suspended Colloids

WILEY-VCH

www.chemelectrochem.org

A Journal of

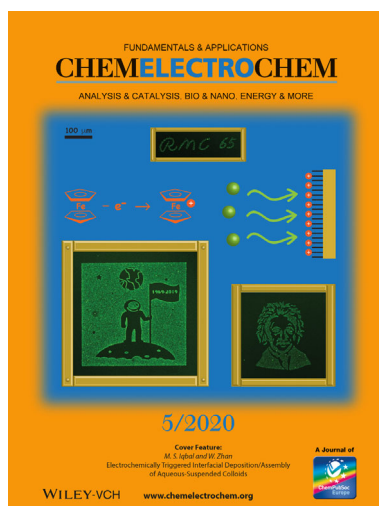


COVER PICTURE

M. S. Iqbal, W. Zhan*



Electrochemically Triggered Interfacial Deposition/Assembly of Aqueous-Suspended Colloids



The Cover Feature shows fluorescence micropatterns (Moon landing, Einstein and the 'Theme logo' designed for this special issue) of colloidal particles electrochemically assembled on electrode surfaces using the method reported here. Starting with ferrocene-terminated self-assembled monolayers and aqueous-suspended colloids, these patterns can be formed in seconds. This work expands the utility of ferrocene-based redox-controlled surfaces. More information can be found in the Article by M. S. Iqbal and W. Zhan.

Special
Collection

Electrochemically Triggered Interfacial Deposition/Assembly of Aqueous-Suspended Colloids

Md. Shamim Iqbal and Wei Zhan*[a]

Following our recent work on polyelectrolyte deposition on ferrocene-terminated self-assembled monolayers (*Langmuir* 2018, 34, 12776–12786), we seek in this study to answer the following question: How would aqueous-suspended colloids respond to the same electrochemical trigger – ferrocene oxidation? Using carboxylic-terminated polystyrene nano-/microbeads as a model colloid, we confirm first their transfer to and deposition at such redox-active surfaces. Key factors

involved, including the starting electrode surfaces, colloid size, range/duration of applied potential, and small supporting electrolytes, are examined in detail. A particularly interesting finding among these is the superior efficiency of the electrochemically triggered assembly compared to the electrically driven process. Taking advantage of this feature, we demonstrate fast, high-fidelity colloid micropattern formation on electrodes at the end.

1. Introduction

We report herein a new electrochemical method for facile deposition/assembly of aqueous-suspended colloids on electrode surfaces. Key to the high efficiency of this method are ferrocene (Fc) moieties, which are introduced into the system via self-assembled alkanethiol monolayers (SAMs), and serve as an electrochemical trigger to initiate and control such deposition/assembly processes. With this method, high-fidelity colloid micropatterns can be formed in seconds. This work expands the utility of ferrocene-based redox-controlled surfaces, which was pioneered by the Whitesides group^[1] and has since then seen quite exciting new development in the field of metallopolymer.^[2,3]

Of particular relevance to this work is the research on electrically driven colloidal assembly on planar electrodes.^[4–6] Ordered colloidal assemblies often display interesting photonic, spectroscopic and catalytic properties,^[7–9] which, when interfaced directly with electrodes, can yield novel devices with improved functionality and controllability. In practice, both *d.c.* and *a.c.* electric fields have been commonly employed. Of the former, which is more related to this work, colloidal particles are driven toward the electrodes by one or a combination of the following mechanisms:^[7,10–12] electrophoresis, electroosmosis, and electrohydrodynamic motion. While the experimental setup is usually simple, containing primarily two parallel electrodes with controlled spacing, sorting out these mechanisms can be quite complex. Such complexity arises first of all from the four components typically involved in the assembly process: the colloids, the working electrode (to some extent, the counter electrode as well), the aqueous medium and

supporting electrolytes, which together give rise to at least two interfaces (i.e., electrode/water and colloid/water) with distinctive double-layer structure and charge distribution. Since any perturbation of charge distribution at these interfaces could potentially modify the electrohydrodynamics experienced by the colloids, their movement and assembly are subjected to the influence of not only the electrodes, but also each other. The latter effect is exemplified by the interesting observation of entrainment of colloidal particles,^[13,14] yielding well-ordered 2D colloidal crystals on electrodes.

In the majority of existing work on electrically-driven formation of colloidal assemblies, faradaic electrode processes are not explicitly considered.^[15,16] This is not an oversight in practice, of course, considering the largely physical nature of the involved mechanisms driving such formations. Of the few studies^[17,18] in which the impact of faradaic reactions is specifically examined, the discussion has been primarily focused on the background redox processes, i.e., water hydrolysis. Nonetheless, it is clear that faradaic reactions can have a deciding influence on the electrokinetic and electrohydrodynamic behaviors^[15,16,19] of aqueous systems. Understanding these behaviors, accordingly, will uncover new ways of controlling and improving colloidal deposition under such settings.

In this work, we studied the deposition/assembly behavior of negatively-charged colloidal particles on planar gold working electrodes grafted with ferrocene-terminated alkanethiol SAMs. This work follows our recent discovery^[20] that polyelectrolytes can be deposited onto these SAMs upon Fc oxidation, which switches the SAM from a hydrophobic surface to positively-charged surface. We demonstrate that this drastic change of surface characteristics can be quite generally applied to initiate and control interfacial deposition and assembly of aqueous-suspended colloidal particles. Key factors involved, including the starting electrode surfaces, colloid size, range/duration of the applied potential, and small supporting electrolytes, are examined in detail, using voltammetry, confocal fluorescence microscopy and quartz crystal microbalance. A particularly

[a] M. S. Iqbal, Prof. Dr. W. Zhan
Department of Chemistry and Biochemistry
Auburn University, Auburn, AL 36849, USA
E-mail: wzz0001@auburn.edu



Supporting information for this article is available on the WWW under <https://doi.org/10.1002/celc.201902143>



An invited contribution to the Richard M. Crooks Festschrift

interesting finding among these is the superior efficiency of the electrochemically triggered assembly compared to the electrically driven process, which we utilize to form high-fidelity colloid micropatterns on electrodes. A detailed discussion on the deposition mechanisms is also provided.

2. Results and Discussion

2.1. Experimental Setup and Background Electrode Responses

Figure 1a depicts schematically the experimental setup employed in this work. At the top is a Teflon cell, which contains a cylindrical through-hole as the solution reservoir at the center and two smaller slant side holes housing a Ag/AgCl reference electrode and a Pt wire counter electrode. The ring-shaped Pt wire is positioned roughly in parallel with the bottom gold-film working electrode, 0.3 cm above. As colloidal samples, carboxylate polystyrene (PS-COOH) beads of six different sizes suspended in DI water, with/without additional supporting electrolytes, were employed. These beads are fluorescently labeled so their deposition/assembly at the semi-transparent

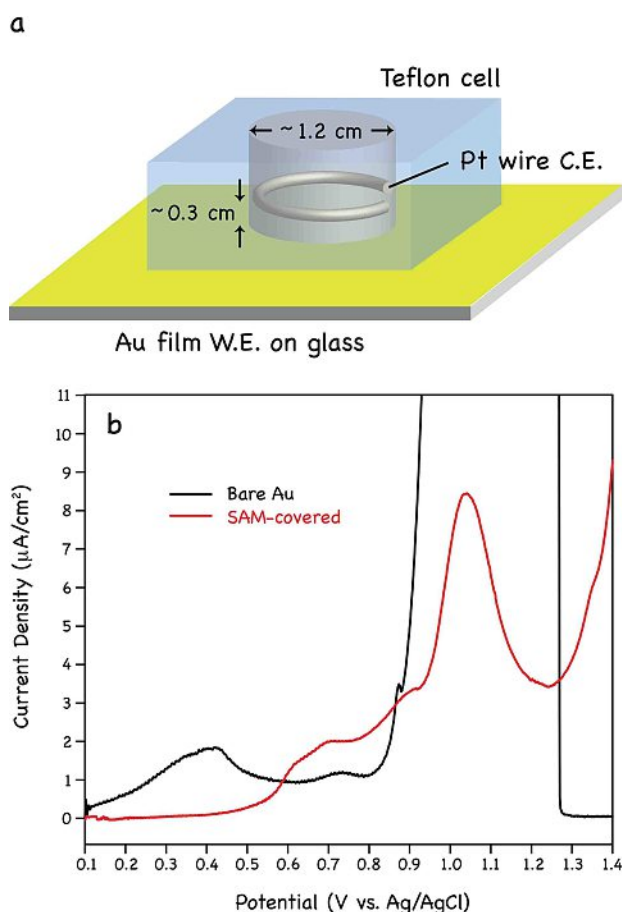


Figure 1. a) Schematic of the three-electrode experimental setup. For clarity, the Ag/AgCl reference electrode and assembly sockets are not included in the drawing. b) Background electrochemical processes probed in DI water using either bare or 1:1 Fc-C11SH/C12SH mixed SAM-covered gold films as working electrode.

gold film electrodes can be fully followed with fluorescence microscopy. Besides size, these beads also differ each other in surface –COOH density, which is reflected by their various zeta potentials that range from –20 to –70 mV (Table 1).

To identify the background electrochemical responses, we first ran linear sweep voltammetry (LSV) with this setup filled with DI water alone. With bare Au films as the working electrode, this yielded an *i*-*V* curve containing three main redox features (Figure 1b, voltammogram in black). The first two broad peaks between 0.4 and 0.8 V appear to correspond to the monolayer and multilayer gold oxide formation,^[21,22] whereas the rise in current past 0.9 V is associated with oxygen evolution. The latter process apparently overloads the 10-nm-thick Au films, causing their complete strip-off from the glass slides evident to the naked eye (not shown). With the film gone, the cell loses its electrical contact past 1.3 V. For Au films covered with 1:1 Fc-C11SH/C12SH mixed SAMs, on the other hand, a quite distinctive LSV profile results (Figure 1b, voltammogram in red). Here, the first pair of redox features are shifted to more positive potentials by about 0.2 V, likely a result of the SAM shielding the Au surface from water and thus hindering gold oxide formation. Following this pair is a prominent, symmetrical wave between 0.9 and 1.2 V, which can be attributed to the delayed Fc oxidation. Comparing the magnitude of this wave with that obtained in NaClO₄ (see below), it appears that this feature contains in addition some other background processes, perhaps e.g., continual oxide formation. After 1.2 V, the oxygen evolution sets in once again.

2.2. Fluorescence Microscopy Confirmation of Colloidal Deposition

With the background processes established, we next examined the deposition behavior of 0.5-μm-diameter PS-COOH beads using bare Au films as the working electrode. As evident from Figure 2a, a submonolayer deposition of randomly distributed beads occurred readily when the electrode was biased by a linear potential sweep from 0.1 to 0.4 V vs. Ag/AgCl. The main redox feature within this potential window roughly coincides with that observed from bare Au probed in water alone (Figure 1b), but with an intensified current output. A similar deposition results when the bias is extended to 0.7 V, within which a small but discernable wave appears at about 0.6 V.

Table 1. General properties of carboxylate polystyrene (PS-COOH) beads studied.

Size [μm]	Parking area ^[a]	Zeta potential [mV]	Bead concentration ^[c]
0.06	57.2	–20.9 ± 2.2 ^[b]	9.58 × 10 ¹⁰
0.22	30.2	–36.3 ± 0.7 ^[b]	2.39 × 10 ¹⁰
0.51	9.4	–35.6 ± 0.5 ^[b]	9.58 × 10 ⁹
1.0	21.8	–49.4 ± 0.4 ^[b]	4.78 × 10 ⁹
2.19	186.2	–51.0 ± 2.1 ^[b]	4.28 × 10 ⁸
4.95	23.8	–69.1 ± 0.7 ^[b]	1.40 × 10 ⁷

[a] Average surface area (Å²) corresponding to each –COOH group, manufacturer's data. [b] Standard deviation, *n* = 3. [c] Count of beads per mL of samples employed in Figure 6.

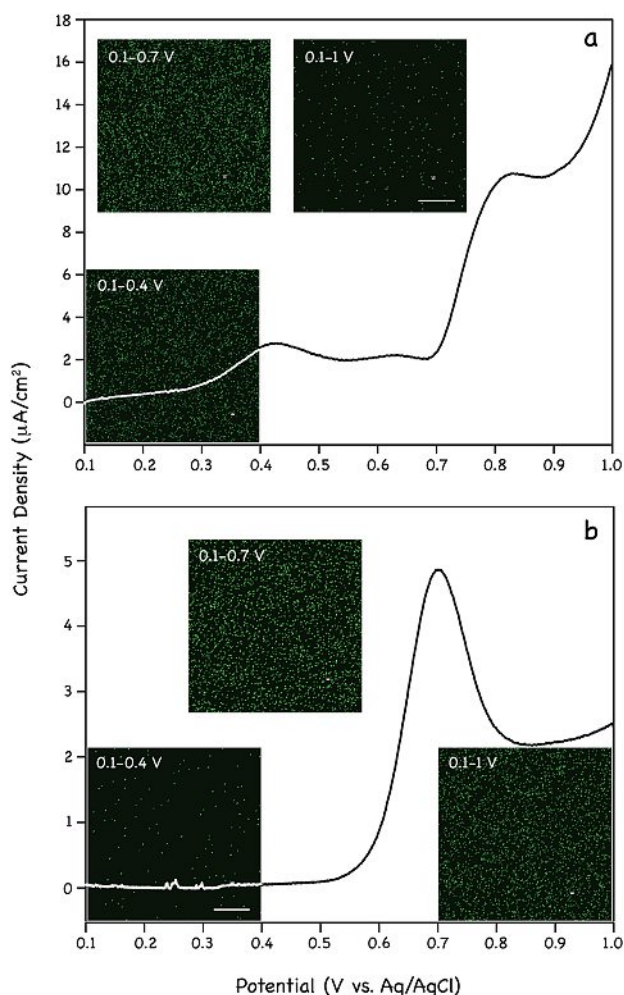


Figure 2. Linear sweep voltammograms (LSV) recorded on either bare gold films (a) or gold films covered with 1:1 Fc-C11SH/C12SH mixed SAMs (b) in aqueous suspensions of 0.5- μm PS-COOH beads (concentration: ca. 1×10^9 per mL). The suspensions in addition contain 0.05 % (w/v) TWEEN 20; scan rate: 10 mV/s. The embedded fluorescence images in each case are obtained from three separate potential scans covering 0.1–0.4 V, 0.1–0.7 V, and 0.1–1 V, respectively. Only the LSVs of 0.1–1 V are shown here; the two short scans overlap with the corresponding segments of the former and are omitted for clarity. The scale bar represents 50 μm and applies to all images.

Immediately following this wave, the current rises significantly, which, after a brief plateau, is substituted by the oxygen evolution reaction at about 0.9 V. Because this feature is absent from the background responses and prior to it microbead deposition has already occurred, we tentatively assign it as expedited Au oxide formation facilitated by the PS-COOH microbeads on-electrode. Since the oxygen evolution causes the Au film to dissolve, the majority of the deposited microbeads are removed from the surface at the end of the 0.1–1 V scan.

Similar tests were then run on Au films covered with 1:1 Fc-C11SH/C12SH mixed SAMs. The SAM modification of the working electrode completely alters the redox processes in operation and hence the course of colloid deposition. Starting off, the relatively quiet electrochemical process within 0.1–0.4 V only led to low-level colloid deposition, whereas submonolayer

colloid depositions with coverage comparable to that seen on bare gold were obtained in the next two potential windows (Figure 2b). The stable deposition obtained from 0.1–1 V scan apparently benefited from the shielding/protection of Au films by the SAM. In the entire scan, there exists only one main electrochemical wave, which starts to rise past 0.5 V and subsequently peaks at 0.7 V. This feature results from the superimposition of at least two redox processes: Au oxide formation (Figure 1b) and Fc SAM oxidation. The latter process, as will be elaborated in more detail later, is compensated mostly by chloride ions leaked into the solution from the Ag/AgCl reference electrode.

While the fluorescence images in Figure 2 (as well as elsewhere in the main text) are taken using a 10x objective lens focused near the center of Au electrodes, low-magnification (4x) imaging was also performed on above samples to cover larger areas of colloidal deposits (SI Figure 1). These images display radially distributed microbead patterns, clearly due to the ring-shaped Pt wire C.E. that causes distortion of the electric field. The patterns formed on bare electrodes are very distinguishable from those on SAM-covered electrodes; the uniform coverage achieved on the latter after 0.1–1 V LSV scan is also evident.

2.3. Electrochemical QCM Characterization of Deposition

To further characterize these colloid deposition processes, we also carried out electrochemical quartz crystal microbalance (QCM) analysis. By employing Au films directly coated on crystal disks as the working electrode, this technique reveals the mass change on the electrode in real time as the associated electrochemical process takes place.^[23] For the bare Au electrode probed in water alone (Figure 3, black trace), the crystal oscillation frequency tips downward shortly after the inauguration of the LSV scan, indicating a mass gain on the electrode that is likely due to the oxide formation on the gold film. The frequency decrease continues at a slow pace before reaching a plateau after 0.7 V vs. Ag/AgCl. When the system is in addition suspended with 0.5 μm PS-COOH beads, the same LSV scan produces a frequency profile with greater downward shift, which can be assigned to the accompanying colloid deposition on the electrode (Figure 3, gray trace). The concurrency of frequency change shown by the two profiles, moreover, indicates a likely connection between Au oxide formation and bead deposition. To be consistent with the conventional nomenclature and distinguish it from the Fc-SAM based process, however, we describe colloidal assemblies formed on bare Au as electrical deposition throughout this work.

Similar tests once again were carried out on Au films covered with 1:1 Fc-C11SH/C12SH mixed SAMs. Here, several deviations are apparent. 1) Onset potential for frequency downshift. Due to suppression of gold oxidation by the SAM, the crystal oscillation frequencies do not shift downward appreciably until 0.4 V (in water alone) or past 0.5 V (in colloid aqueous suspensions), matching well with the LSV results (Figures 1b and 2b); 2) Correspondence between the colloid

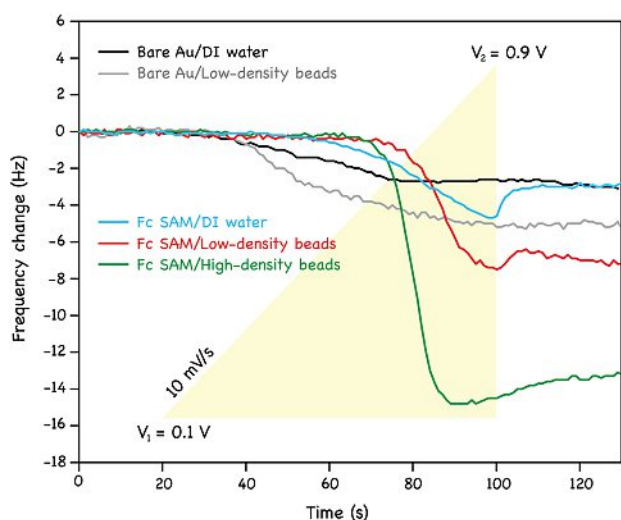


Figure 3. Electrochemical QCM monitoring of deposition of 0.5 μm PS-COOH beads (low-density: ca. 1×10^7 per mL vs. high density: ca. 1×10^9 per mL) on either bare gold electrodes or gold electrodes covered with 1:1 Fc-C11SH/C12SH mixed SAMs. The samples in addition contain 0.05% (w/v) TWEEN 20. In each case, the gold electrodes were biased by a linear potential scan from 0.1 to 0.9 V at 10 mV/s, as marked by the yellow triangle.

deposition and Fc oxidation. The steepest frequency decreases coincide with the voltammetric peak of Fc oxidation, which strongly suggests the latter process is responsible for the observed deposition; 3) Magnitude/speed of frequency shifts. For the same concentration of suspended PS-COOH microbeads, the frequency shift takes place more steeply on SAM-covered electrode than on the bare electrode. A $>60\%$ higher downshift was also observed on SAM-covered electrode (Figure 3, red vs. gray traces) at the end of the LSV scan; 4) Dependence of deposition on colloid concentration. When the bead density was increased from 1×10^7 to 1×10^9 per mL, an approximate doubling of frequency downshift was registered. In the latter case, a frequency minimum was reached before the end of the scan (~ 0.8 V), suggesting faster bead deposition and saturation on the SAM. A similar trend was also shown by the accompanying resistance change profiles: greater resistance upshifts on Fc-SAMs and in the presence of a higher concentration of beads (SI Figure 2).

2.4. Simultaneous Electrochemical and Electrical Deposition

With the results presented above establishing colloidal deposition on both SAM-covered electrodes and bare electrodes, an interesting question emerges: Are they the same or different processes? To answer this question, we next employed Au films partially covered with SAMs so that the two formats of deposition can be run side-by-side on the same electrode. To achieve such partial coverage, we chose to graft the thiols onto the bare Au electrodes via a pre-patterned silicone rubber stamp, using the microcontact printing (μCP)^[24] technique initially developed by the Whitesides group. As shown schematically in Figure 4a, the stamp carries positive features of

a 10- μm -diameter micropillar array with 10 μm spacing, which, upon printing, will yield SAM patterns with the same shape/dimension on the electrodes.

As before, we ran LSV scans on these thiol-patterned Au film electrodes in three potential windows in 0.5 μm -diameter PS-COOH bead aqueous suspensions. Upon the initial 0.1–0.4 V sweep, strikingly, a microbead array that reproduces the original pattern on the stamp results (Figure 4b). Despite their low coverage, the fact that the beads only land on spots where the thiols are put down via μCP is unmistakable. Such exclusive deposition becomes more evident as a result of more extended potential scans (Figure 4c, d), yielding on average 3–5 beads per SAM micropatch after the 0.1–0.7 V run and 7–10 beads after the 0.1–1 V run. Since deposition occurs more efficiently on bare Au alone than on SAM-covered electrodes in the potential window of 0.1–0.4 V (Figure 2), it follows that the thiol anchorage on gold completely disables the remaining open Au surface from recruiting microbeads. We will defer a detailed discussion of involved mechanisms till a later section.

2.5. Effect of Supporting Electrolyte

To better understand the electrohydrodynamic characteristics of these colloidal particles during Fc SAM oxidation, we then chose to examine a series of parameters critically involved in the deposition process. This started with small supporting electrolyte, in which we examined how the presence of either NaClO_4 or NaCl in the system would influence the deposition. Of the two, perchlorate stands clearly as the electrolyte of choice for probing Fc SAM electrochemistry, owing to its low hydration that leads to strong ion-pairing with ferrocenium.^[25,26] In comparison, the highly solvated chloride ions^[26] are less effective in accommodating the Fc/Fc^+ transition, giving rise to a higher Fc oxidation potential.

When the SAM-modified Au film electrodes were probed in 0.1 M NaClO_4 (together with 0.5- μm -diameter PS-COOH beads), a typical bell-shaped Fc SAM oxidation voltammogram was obtained^[27] (Figure 5). Remarkably, a $>80\%$ decrease in the bead coverage was detected on the electrode compared to that obtained in DI water after the 0.1–0.7 V scan (Figure 2b), which indicates NaClO_4 can effectively suppress colloid deposition. In contrast, colloidal deposition proceeds largely undisturbed in the presence of 0.1 M NaCl (Figure 5), which remains the case even when the NaCl concentration is raised to 2 M (SI Figure 3). Taken together, these results strongly suggest the direct involvement of ferrocenium in driving colloidal deposition, whose neutralization by perchlorate (but not chloride) effectively abolishes the deposition process.

On the other hand, the voltammogram obtained in 0.1 M NaCl matches the one shown in Figure 2b closely in shape and peak position, confirming that chloride ions are also responsible for charge compensation in the earlier case.

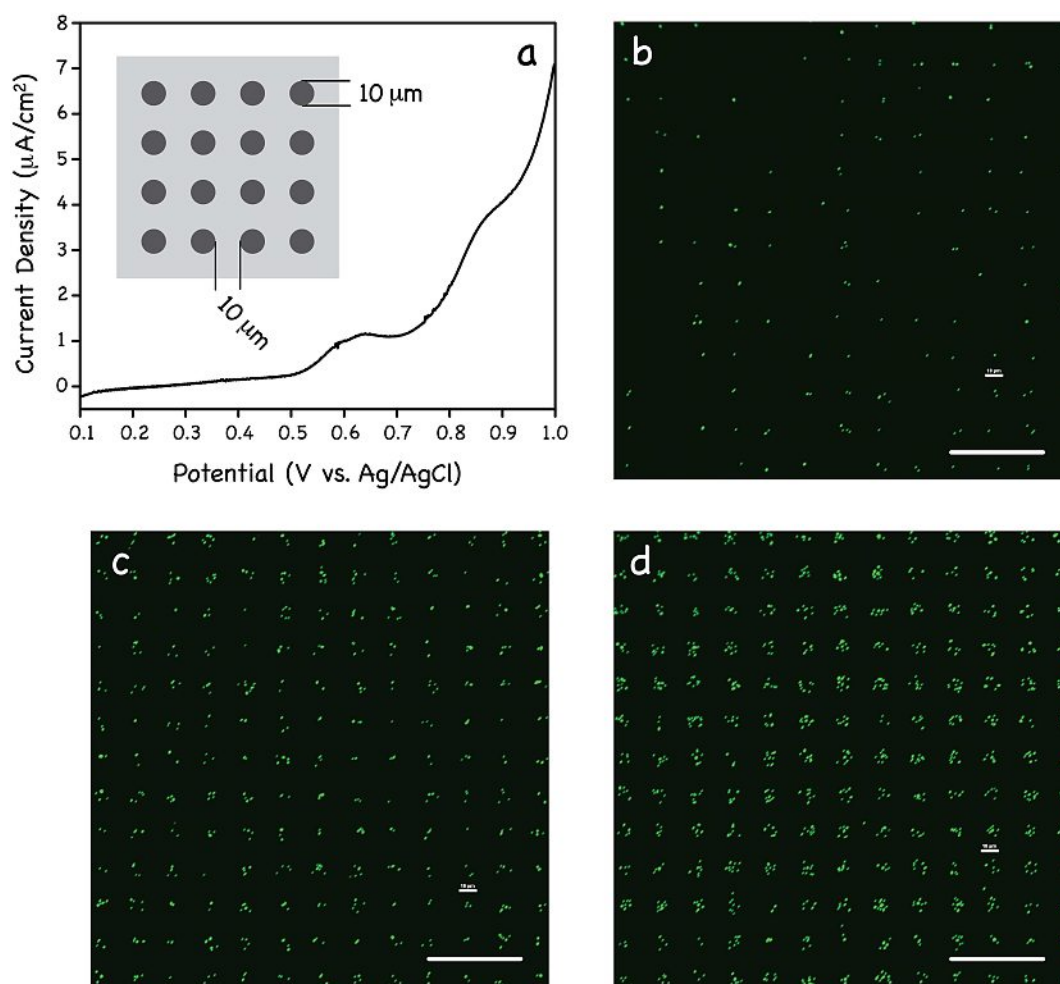


Figure 4. a) Linear sweep voltammogram of patterned 1:1 Fc-C11SH/C12SH mixed SAMs probed in 0.5 μm PS-COOH microbead aqueous suspensions (concentration: $\sim 1 \times 10^9$ per mL, with 0.05 % (w/v) TWEEN 20). Inset: schematic depiction of the layout and dimensions of the microarray employed in microcontact printing of thiols. See the Experimental section for more details. b) to d) Fluorescence images of gold film electrodes covered with 1:1 Fc-C11SH/C12SH mixed SAM micropatterns after a single LSV scan from 0.1 to 0.4 V (b), 0.1 to 0.7 V (c), and 0.1 to 1 V (d), in 0.5 μm microbead aqueous suspensions. Potential scan rate: 10 mV/s; scale bar: 50 μm .

2.6. Effect of Colloid Size

To further shed light on the deposition mechanisms, we also extended the above characterization procedure to 5 other PS-COOH bead samples, which together cover two orders of colloid size. The fluorescence imaging results of the deposited PS-COOH beads are shown in Figure 6. Among these, the 60-nm beads are not individually resolved due to their small size, resulting in a relatively weak, continuous fluorescent image. As will become evident later, their deposition has successfully occurred nevertheless. In general, as the size of colloids increases, their distribution becomes less even. This trend is most evident for the 2- μm and 5- μm samples, in which cases most deposited particles actually exist in clusters. The coverage of these two microbeads on electrodes is also noticeably lower than other samples. Factors that may cause such characteristic formations will be discussed in a later section.

2.7. Effect of Scan Rate

Finally, we examined the effect of LSV scan rate on the colloid deposition. As summarized in Table 2, comparable deposition was obtained at relatively slow scan rates, i.e., between 10 mV/s and 100 mV/s, for 0.5- μm PS-COOH beads; as the scan rate increases further, a steady decrease of colloid surface coverage

Table 2. Scan rate dependence of electrochemically triggered deposition of 0.5- μm -diameter PS-COOH beads.

Scan rate [mV/s] ^[a]	Particle coverage [%]	Particle count
10	$8.9 \pm 0.7^{[b]}$	$3127 \pm 138^{[b]}$
100	$9.4 \pm 0.3^{[b]}$	$2955 \pm 114^{[b]}$
250	$6.8 \pm 0.5^{[b]}$	$1896 \pm 97^{[b]}$
500	$3.7 \pm 0.2^{[b]}$	$847 \pm 48^{[b]}$
1000	$2.2 \pm 0.5^{[b]}$	$559 \pm 147^{[b]}$

[a] Results obtained from a single LSV scan from 0.1 to 0.8 V; bead concentration: 9.58×10^9 per mL. [b] Standard deviation, $n = 3$ or 4.

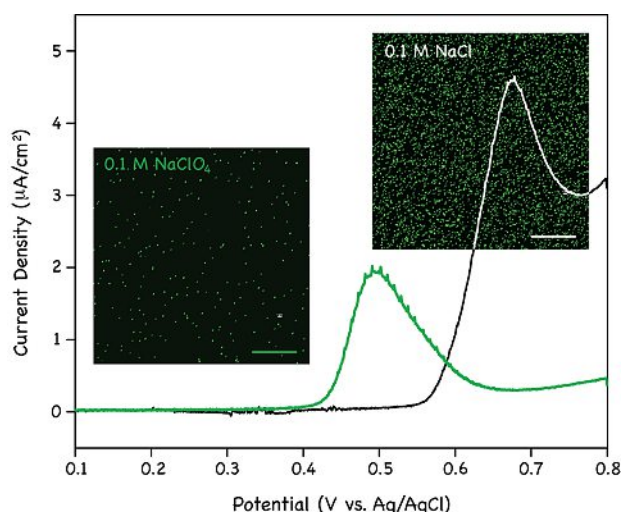


Figure 5. Linear sweep voltammograms of 1:1 Fc-C11SH/C12SH mixed SAMs probed in 0.5 μm PS-COOH microbead aqueous suspensions (bead concentration: ca. 1×10^9 per mL, 0.05 % (w/v) TWEEN 20) in the presence of either 0.1 M NaClO_4 (green) or 0.1 M NaCl (black and white). Inset: fluorescence images of the SAM-covered gold surfaces following the LSV treatments. Potential scan rate: 10 mV/s; scale bar: 50 μm .

results. At the highest scan rate tested, 1 V/s, for example, the count of deposited particles drops by > 80% compared to that obtained at 10 mV/s and 100 mV/s. Using the latter rate as the threshold at which the colloid mass transfer limit (by diffusion)

sets in, we can roughly estimate a timescale of a few seconds, i.e., the minimum time needed for a full-extent deposition of 0.5 μm PS-COOH beads on 1:1 Fc-C11SH/C12SH mixed SAMs.

2.8. Deposition Mechanisms

With all the characterization results presented above, we now attempt a preliminary and qualitative analysis of the involved deposition mechanisms in this section.

1) Magnitude and Distribution of the Electric Field

In order to assess the relative contribution of each possible mode of motion, it is helpful to first establish the size/distribution of electric field (E) present in our system. For that, we need to know the potential drop on both working and counter electrodes. For the latter, we take the value of -0.6 V vs. Ag/AgCl, assuming $2\text{H}^+ + 2\text{e}^- = \text{H}_2$ under neutral pH as the redox process occurring on the Pt wire.^[28] Taking the peak potentials on working electrodes to be 0.4 V (bare Au, Figure 2) and 0.7 V (SAM-covered Au, Figure 2), respectively, and the distance between W.E. and C.E. to be 0.3 cm (Figure 1), we can roughly estimate their corresponding apparent electric field: 3.3 and 4.3 V/cm. It is important to note once again that the electric field is not uniform in either case (SI Figure 1).

As discussed above, significant concentrations of KCl were expected to be present in the colloidal suspensions due to its leakage from the reference electrode. This condition gives rises

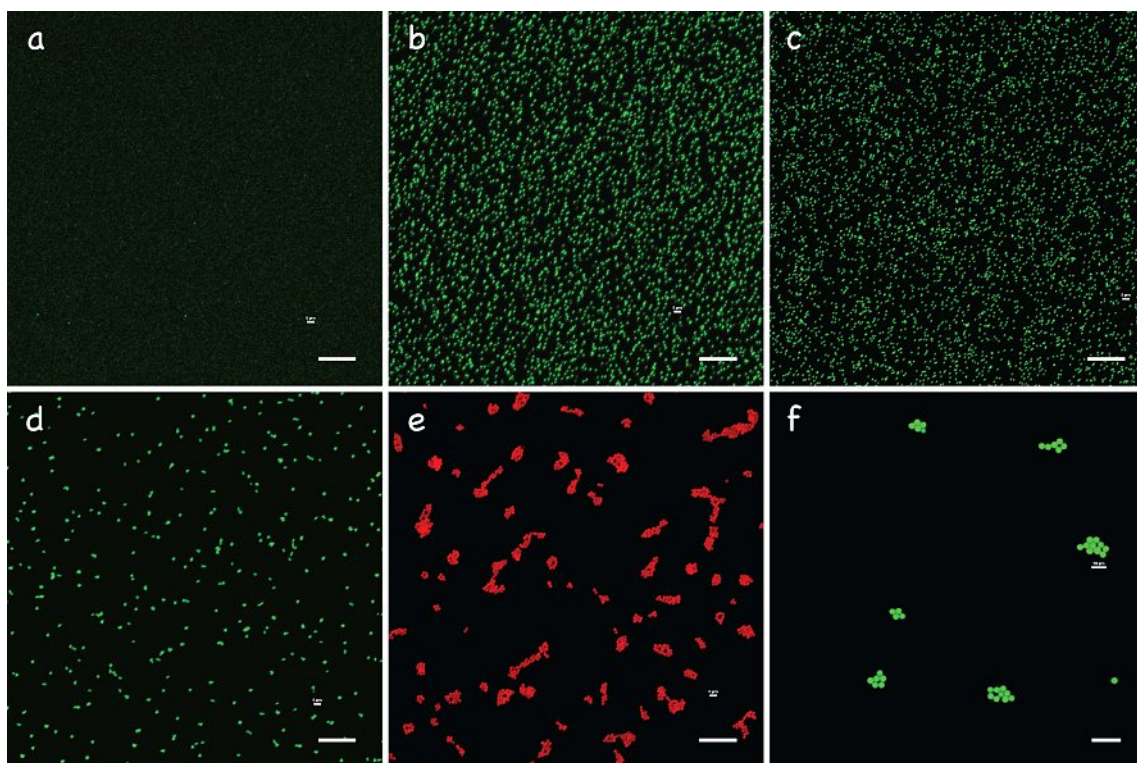


Figure 6. Fluorescence images of electrochemically triggered deposition of PS-COOH beads of various sizes on 1:1 Fc-C11SH/C12SH mixed SAMs. Bead size: a) 0.06 μm , b) 0.22 μm , c) 0.51 μm , d) 1.0 μm , e) 2.19 μm and f) 4.95 μm ; their concentrations are specified in Table 1. All samples were treated by a single LSV scan from 0.1 to 0.8 V at 10 mV/s. The scale bars correspond to 50 μm .

to a thin double-layer surrounding the PS-COOH beads, i.e., with their Debye length expected to be on the order of nm.^[29] By contrast, the double-layer structure associated with the electrode prior to the potential sweep is less well-defined due mainly to the hydrophobicity of the SAM surface.

2) Classical/Linear Electrophoretic Motion of Colloidal Particles

As the linear potential sweep is switched on, an electric field starts to develop between the W.E. and C.E., to which the negatively charged colloidal particles have to respond with electrophoretic motion. The resultant electrophoretic mobility (μ) can be estimated from the zeta potential of the colloid according to the Helmholtz-Smoluchowski equation:^[30] $\mu = \epsilon_0 \epsilon \zeta / \eta$, in which ζ is the zeta potential of the particle, ϵ_0 the vacuum permittivity, ϵ and η are respectively the relative dielectric permittivity and viscosity of the medium. From the zeta potential measured for the 0.5 μm PS-COOH beads, -35.6 mV (Table 1), we then obtain μ at $-2.5 \times 10^{-4} \text{ cm}^2 \text{V}^{-1} \text{s}^{-1}$, which, under the pertinent electric field, corresponds to a scenario where a microbead migrates at most 10 μm a second. On the other hand, if the bead movement is driven by such electrophoresis alone, longer runs should always result in more extensive deposition. The fact that this is not the case, e.g., in 10 mV/s vs. 100 mV/s depositions, therefore, points to the likely presence of other driving mechanism(s) in the current system.

3) Faradaic-Charge-Induced Electrophoresis and Electroosmosis

Upon Fc oxidation, a positively charged layer starts to emerge at the SAM/water interface. This instantaneously triggers an influx of anions toward the SAM-covered electrode, which in turn creates a region near the surface where surface cations (i.e., ferrocenium) and the incoming anions are separated in space. As the oxidative current continues to develop, this zone of charge imbalance expands further into the bulk, producing a double-layer that is considerably thicker than normal. The physical significance of this dipolar zone lies in that 1) it imposes a second electric field on top of the external electric field and 2) the electrostatic interactions between the two fields create a whole new series of electrokinetic flows in the system. To begin with, a secondary electrophoretic motion arises because this bulk charge region directly modifies the charge distribution on the surface of colloidal particles dispersed within (Figure 7). Similarly, any tangential field component existing in the system can cause the incoming counter anions to slip at the SAM surface, i.e., electroosmotic flow (EOF), which in turn triggers circulating fluid movement capable of carrying the suspended colloids toward the electrode surface (Figure 7).

According to the existing theoretical models on induced-charge electroosmosis^[15,16] as well as the 'electrokinetic phenomena of the second kind',^[31,32] the velocity (u) of such induced electrokinetic flows generally takes the nonlinear Smoluchowski form, $u \propto \epsilon_0 \epsilon E E_i / \eta$, where E and E_i are the primary and induced electric field components, respectively, and a the particle radius. In comparison to the linear Smoluchowski formula,^[30] here E_i appears in place of ζ , whereas the new term, a , marks the size-dependent nature of such flows. Of the former, it is precisely because E_i can be substantially larger than ζ that these secondary electrokinetic

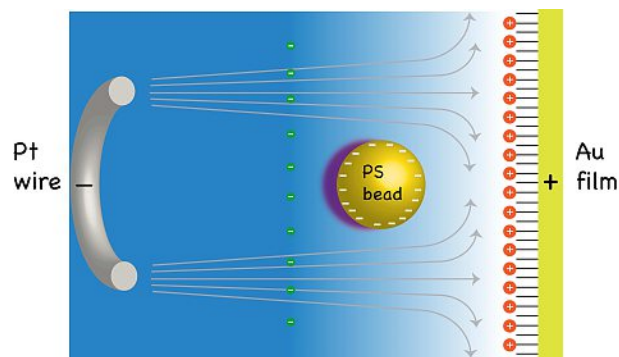


Figure 7. Schematic illustration of some key mechanistic features of the electrochemically triggered deposition. Following Figure 1 (with 90° rotation), the primary electric field is established between Au film W.E. and Pt wire C.E. Upon Fc-SAM oxidation, a secondary field also develops between the Fc^+ layer (orange circles with embedded plus signs) and the front of the counterion influx (green circles with embedded minus signs). Colloidal particles (one shown in gold) situated within this zone are subjected to the influence of both fields, whose interactions generate secondary electrokinetic flows. The drop shadow in purple depicts the distorted diffuse layer of the bead particularly caused by the local secondary electric field; arrowed lines in gray are idealized streamlines of the flow pattern.

flows sometimes exceed the classical motions in velocity by several orders of magnitude.^[31,32] On the other hand, it is tempting to attribute the observed clustering of large microbeads (2 μm and 5 μm , Figure 6) to the size dependence predicted of these nonlinear induced electrokinetic flows. Their low surface coverage, on the other hand, is likely due to a combination of the following two factors: their lower starting concentrations (Table 1) and slower diffusion. The latter process scales with $1/a$ and is expected to pose a more severe mass-transfer limit on these larger beads once they are depleted near the electrode by the secondary electrokinetic flows. This attribution is also in line with the different impacts on the colloidal deposition observed between ClO_4^- and Cl^- (Figure 5): due to its strong ion-pairing with Fc^+ , ClO_4^- does not effectively sustain EOF. Without EOF carrying the microbeads toward the electrode, accordingly, the resulting deposition is greatly suppressed.

Extrapolating from the observations above, we can see easily the likely importance of many other factors associated with the Faradaic processes, such as type/kinetics of the involved electrochemical reaction(s), in the colloidal deposition. For instance, although gold oxidation itself is sufficient to trigger deposition on bare Au electrodes (Figure 2a), it is sluggish and does not produce nearly as much charge as the competing reaction, $\text{Fc} - e^- = \text{Fc}^+$. These enable the latter reaction to sustain secondary electrokinetic flows much more strongly, which in turn lead to faster colloid deposition (Figure 3) and a complete dominance over the gold-oxidation based process (Figure 4).

4) The Actual Deposition and Post-deposition Stability

Another conclusion we may draw from the discussion so far is that Faradaic reactions can accelerate the arrival of colloidal particles at the electrode. Mechanically, this fast motion may lead to a 'hard landing' scenario, in which the momentum due to colloid stoppage at the surface may afford the particle a

closer contact with the SAM and hence more intimate electrostatic and van der Waal interactions than otherwise possible. Of course, with the colloid's fixed surface charge releasing small ions and water into the bulk, the deposition process also leads to an entropy gain of the system. These considerations help explain the observation of irreversibly surface adhesion of microbeads following electrochemically triggered deposition. For example, the deposited beads can withstand typical washing steps well and do not come off the electrode until we electrochemically desorb the SAM underneath at -2.0 V vs. Ag/AgCl (SI Figure 4). By contrast, colloidal formations driven by electrophoretic deposition are often reversible assemblies.^[7] Once the electric field is switched off, a random distribution of the colloidal particles often resumes as a result of Brownian motion; alternatively, the initially deposited colloids can be lifted off from the electrode by reversing the field polarity.

2.9. Electrochemically Triggered Colloid Micropattern Formation on Electrodes: An Application

Taking advantage of the superior efficiency of the electrochemically triggered assembly compared to the electrically driven process, we conclude this investigation with a demonstration of fast, high-fidelity colloid micropattern formation on electrodes. Shown in Figure 8 is a $\sim 200 \times 300$ μm portrait of Einstein formed by 60 nm fluorescent PS-COOH beads electrochemically assembled on a Au film electrode. Fine lines down to just a few microns are satisfactorily resolved. A cartoon rendering of the historical 'Moon Landing' with similar resolution is also included

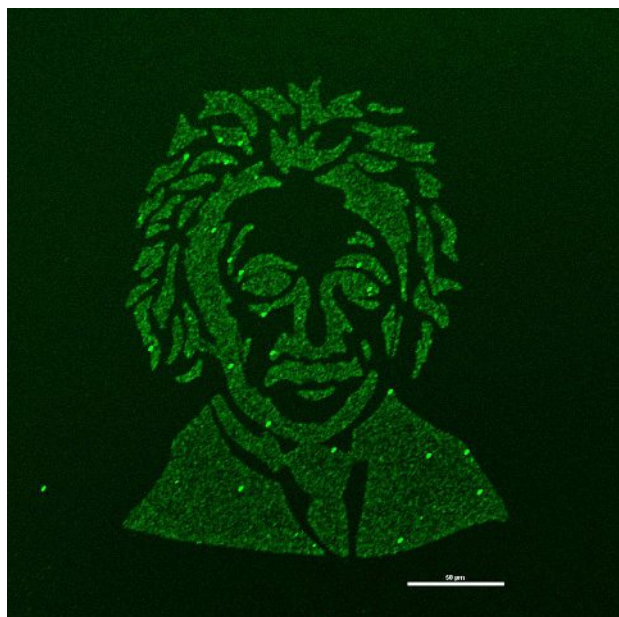


Figure 8. Head portrait of Einstein formed by 0.06 μm green-fluorescent PS-COOH beads assembled on a gold film electrode using our electrochemically triggered approach. Prior to the assembly step, the portrait pattern was first microcontact-printed onto the gold electrode in form of 1:1 Fc-C11SH/C12SH mixed SAMs via a silicone rubber stamp. A linear potential sweep from 0.1 to 0.8 V was then applied at 10 mV/s; scale bar: 50 μm .

as the TOC graphic of this work. Separately, we also attempted similar patterning/assembly using C12SH alone as the ink followed by electrical deposition, which fails to produce any recognizable microbead patterns on the electrode (not shown). This negative control once again illustrates the critical role played by Fc in achieving successful micropattern formation. Using better-resolved stamps and colloids of smaller size, it should be possible to construct still finer features in a similar fashion.

3. Concluding Remarks

Above we have presented a new electrochemical method for efficient and straightforward deposition/assembly of aqueous-suspended colloids on electrode surfaces. Using carboxylic-terminated polystyrene nano-/microbeads as a model colloid, we characterized this electrochemically triggered process in detail; by comparing its performance with conventional, electrically driven processes, we demonstrated superior deposition efficiency achievable with this new method. A qualitative discussion of the involved deposition mechanisms is also given, featuring secondary, induced electrokinetic flows carrying the microbeads toward the electrode surface. To showcase the potential utility of this method, we also demonstrated fast and high-fidelity colloid micropattern formation on electrodes.

The approach described here offers several exciting new possibilities. Fundamentally, adding well-defined faradaic reactions into the deposition process offers a new and largely independent mechanism to induce secondary electric field components. With their great design flexibility, SAMs bring a new dimension into controlling/tuning various physicochemical parameters involved in the deposition process. Through control of Fc density in the SAMs, for instance, one can easily access a range of surface potentials following the same preparation procedure. Since all redox-active materials are surface-bound, importantly, such gains in control and efficiency are achieved without complicating/compromising the solution phase. On the other hand, the low-voltage and fast operation characteristic of this approach should make it an appealing alternative for applications involving colloidal assemblies.^[7–9] Auxiliary techniques amenable to the SAM formation, such as microcontact printing we employed here, will certainly extend the level of control and sophistication of these practices further. Work is ongoing in our laboratory to explore some of these possibilities.

Experimental Details

Chemicals

11-Ferrocenyl-1-undecanethiol (Fc-C11SH), 1-dodecanethiol (C12SH), sodium perchlorate hydrate (99.99% trace metal basis), sodium chloride ($\geq 99.5\%$), TWEEN 20 were products of Sigma-Aldrich (St. Louis, MO). Fluorescent carboxylate-modified polystyrene nanospheres/microspheres were obtained from Bangs Laboratories, Inc. (Fishers, IN). Deionized water of 18.2 M Ω -cm (Millipore)

was used in preparing all aqueous colloid suspensions as well as in all rinsing and dilution steps.

Formation of Self-Assembled Monolayers

Self-assembled monolayers (SAMs) containing Fc–C11SH/C12SH binary mixtures formed on semi-transparent gold-coated microscope slides (Au thickness: 10 nm, Sigma-Aldrich) were used throughout this work. These SAMs were prepared in two fashions as follows:

1) Solution Incubation

Prior to the SAM formation, gold-coated substrates were immersed in a piranha solution (3:1 v/v mixture of concentrated H₂SO₄ and H₂O₂ 30 wt% aqueous solution) for 3 min, thoroughly rinsed with deionized water, ethanol, and then dried under N₂. Thus cleaned dry substrates were immediately immersed in an ethanol solution containing 0.5 mM Fc–C11SH and C12SH each; the incubation was allowed to proceed for 16–18 h in the dark. Upon completion, the substrates were rinsed first with methanol to remove excess thiols on surface, then DI water, and finally dried under N₂. These SAM-covered gold slides were normally used within the same day of their preparation.

2) Microcontact Printing

Silicone rubber stamps, containing either circular pillar arrays or custom micropatterns, were obtained from Research Micro Stamps (Clemson, SC). Of the latter, hand-drawn features were first converted to digital files with a digital camera and shrunk to desired sizes in Adobe Illustrator (version: CS6); the resulting miniaturized patterns were saved in .svg format and subsequently passed to the manufacturer for stamp production. Before use, the stamps were first cleaned by sonicating in ethanol for 5 min, and gently dried under a stream of N₂. To ink, thus cleaned stamps were soaked in an ethanol solution of 0.5 mM Fc–C11SH and C12SH each for 10 min and then gently dried under N₂. Immediately afterwards, these inked stamps were placed conformally onto precleaned gold-coated glass slides; the printing was allowed to proceed for 10 min, during which a small weight block was placed on top of the stamp to ensure a gentle and even press. Upon completion, the stamps were removed, and the substrates were thoroughly rinsed with methanol, then DI water, and dried under N₂. These SAM-patterned gold slides were normally used within the same day of their preparation.

Electrochemical Treatments and Characterization

Linear sweep voltammetry (LSV) operated by a PC-controlled potentiostat (CHI 910B, CH Instruments, Austin, TX) was used in this work to initiate colloidal deposition and assembly on electrodes. A three-electrode setup was used throughout this work, consisting SAM-covered gold substrates as the working electrode, a platinum wire (diameter: 1 mm) as the counter electrode and Ag/AgCl in saturated KCl solution as the reference electrode, housed in homemade Teflon cells (Figure 1). To initiate the deposition, a given SAM was typically biased with an LSV scan in an intended colloid suspension in 0.05% (w/v) aqueous solution of TWEEN 20. After LSV scan, the initial suspension was thoroughly exchanged out with deionized water, and the gold electrode thus treated was taken out and dried under a gentle stream of ultrapure N₂. Deposits can also be formed from colloids suspended in DI water without adding TWEEN 20 but with a slightly inferior reproducibility.

Zeta Potential Measurements

Zeta potential values of polystyrene nanobeads and microbeads suspended in DI water were obtained from a Malvern Zetasizer (Nano-ZS, Malvern Instruments, Worcestershire, UK) using capillary cells (DTS1070) operated under a 150 V bias at 25 °C. Typically three parallel readings were taken for each sample.

Electrochemical Quartz Crystal Microbalance (EQCM)

EQCM measurements were carried out at room temperature using a QCM analyzer with a 5 MHz crystal oscillator (Model: QCM25) from Stanford Research Systems (Sunnyvale, CA). The quartz crystals used are polished quartz wafers of 1-inch diameter with circular gold electrodes coated on both sides. Before use, these gold-coated quartz crystals were cleaned and grafted with a 1:1 Fc–C11SH/C12SH mixed SAM as described above. The SAM-coated crystal was subsequently mounted on the QCM crystal holder, and its solution-facing electrode was used as the working electrode in a three-electrode configuration together with a Pt-wire counter electrode and a Ag/AgCl reference electrode (in saturated KCl). To do so, a PC controlled potentiostat (CHI 910B, CH Instruments) was connected to the QCM crystal holder via the crystal face bias connector of the QCM25 crystal controller. This setup enables simultaneous monitoring of the QCM frequency shift and current on the working electrode (crystal) as a function of the applied potential; the latter is furnished by the potentiostat in the form of LSV between 0.1 and 0.9 V at 10 mV/s.

Fluorescence Microscopy

Fluorescence images were acquired on a Nikon A1+/MP confocal scanning laser microscope (Nikon Instruments, Inc., Melville, NY) with 4x and 10x objectives. Laser beams at 488 and 561 nm were used to excite green- and red-emitting colloidal bead assemblies formed on semi-transparent gold-coated glass slides, and the corresponding emission signals were filtered at 525 ± 25 and 595 ± 25 nm, respectively.

Acknowledgment

This work is supported in part by the National Science Foundation (award No. CHE-1808123).

Keywords: colloids • electrochemically triggered electrokinetic motion • ferrocene • self-assembled monolayers • redox-controlled surfaces

- [1] N. L. Abbott, G. M. Whitesides, *Langmuir* **1994**, *10*, 1493–1497.
- [2] G. R. Whittell, I. Manners, *Adv. Mater.* **2007**, *19*, 3439–3468.
- [3] M. Gallei, C. Rüttiger, *Chem. Eur. J.* **2018**, *24*, 10006–10021.
- [4] M. Giersig, P. Mulvaney, *Langmuir* **1993**, *9*, 3408–3413.
- [5] M. Trau, D. A. Saville, I. A. Aksay, *Science* **1996**, *272*, 706–709.
- [6] S.-R. Yeh, M. Seul, B. I. Shraiman, *Nature* **1997**, *386*, 57–59.
- [7] D. C. Prieve, J. P. Sides, C. L. Wirth, *Curr. Opin. Colloid Interface Sci.* **2010**, *15*, 160–174.
- [8] Z. Lu, Y. Yin, *Chem. Soc. Rev.* **2012**, *41*, 6874–6887.
- [9] M. A. Boles, M. Engel, D. V. Talapin, *Chem. Rev.* **2016**, *116*, 11220–11289.
- [10] R. W. O'Brien, L. R. White, **1978**, *74*, 1607–1626.
- [11] J. L. Anderson, *Ann. Rev. Fluid Mech.* **1989**, *21*, 61–99.
- [12] Y. Solomentsev, M. Böhmer, J. L. Anderson, *Langmuir* **1997**, *13*, 6358–6368.
- [13] M. Böhmer, *Langmuir* **1996**, *12*, 5747–5750.

- [14] M. Trau, D. A. Saville, I. A. Aksay, *Langmuir* **1997**, *13*, 6375–6381.
- [15] T. M. Squires, M. Z. Bazant, *J. Fluid Mech.* **2004**, *509*, 217–252.
- [16] M. Z. Bazant, T. M. Squires, *Curr. Opin. Colloid Interface Sci.* **2010**, *15*, 203–213.
- [17] R. J. Kershner, J. W. Bullard, M. J. Cima, *J. Colloid Interface Sci.* **2004**, *278*, 146–154.
- [18] W. D. Ristenpart, I. A. Aksay, D. A. Saville, *Langmuir* **2007**, *23*, 4071–4080.
- [19] J. F. L. Duval, G. K. Huijs, W. F. Threels, J. Lyklema, H. P. van Leeuwen, *J. Colloid Interface Sci.* **2003**, *260*, 95–106.
- [20] M. S. Iqbal, W. Zhan, *Langmuir* **2018**, *34*, 12776–12786.
- [21] M. M. Jaksic, B. Johansen, R. Tunold, *Int. J. Hydrogen Energy* **1993**, *18*, 91–110.
- [22] S. J. Xie, V. I. Birss, *J. Electroanal. Chem.* **2001**, *500*, 562–573.
- [23] D. A. Buttry, M. D. Ward, *Chem. Rev.* **1992**, *92*, 1355–1379.
- [24] A. Kumar, H. A. Biebuyck, G. M. Whitesides, *Langmuir* **1994**, *10*, 1498–1511.
- [25] G. K. Rowe, S. E. Creager, *J. Phys. Chem.* **1994**, *98*, 5500–5507.
- [26] G. Valincius, G. Niaura, B. Kazakevičienė, Z. Talaikytė, M. Kažemėkaitė, E. Butkus, V. Razumas, *Langmuir* **2004**, *20*, 6631–6638.
- [27] The peak potential, ~0.5 V vs. Ag/AgCl, is noticeably more positive than the values typically reported in literature, e.g., 0.32 V in our earlier report (ref. 20), which we find is mostly caused by the different electrode configuration employed in this work.
- [28] M. J. N. Pourbaix, J. Van Muylder, N. de Zoubov, *Platinum Met. Rev.* **1959**, *3*, 47–53.
- [29] J. N. Israelachvili, *Intermolecular and Surface Forces*, 3rd ed.; Elsevier Inc.: Amsterdam, The Netherlands, **2011**.
- [30] R. J. Hunter, *Zeta Potential in Colloid Science*, Academic Press Inc.: London, UK, **1981**.
- [31] S. S. Dukhin, *Adv. Colloid Interface Sci.* **1991**, *35*, 173–196.
- [32] A. A. Baran, N. A. Mishchuk, D. C. Prieve, *J. Colloid Interface Sci.* **1998**, *207*, 240–250.

Manuscript received: December 24, 2019

Revised manuscript received: January 17, 2020

Accepted manuscript online: January 26, 2020